

Image Generation Method Based on Heat Diffusion Models

Pengfei Zhang, Shouqing Jia

Abstract— Denoising Diffusion Probabilistic Models (DDPMs) achieve high-quality image generation without adversarial training, but they process images as a whole. Since adjacent pixels are highly likely to belong to the same object, we propose the Heat Diffusion Model (HDM) to further preserve image details and generate more realistic images. HDM is a model that incorporates pixel-level operations while maintaining the same training process as DDPM. In HDM, the discrete form of the two-dimensional heat equation is integrated into the diffusion and generation formulas of DDPM, enabling the model to compute relationships between neighboring pixels during image processing. Our experiments demonstrate that HDM can generate higher-quality samples compared to models such as DDPM, Consistency Diffusion Models (CDM), Latent Diffusion Models (LDM), and Vector Quantized Generative Adversarial Networks (VQGAN).

Index Terms— Denoising Diffusion Probabilistic Models (DDPMs), Heat Diffusion Model (HDM), Image generation, Pixel-level operations, Thermal diffusion, Heat equation.

1 INTRODUCTION

Generative models have demonstrated their capability to produce high-quality samples across numerous domains. Variational Autoencoders (VAEs), and Generative Adversarial Networks (GANs) are increasingly fading from the spotlight[1]. Diffusion-based image generation models have emerged as one of the preferred approaches for addressing challenges in the field of image generation[2]. For example, Denoising Diffusion Probabilistic Models (DDPMs) introduces a stepwise denoising process on the basis of DM, significantly improving the quality of generated images and the stability of training[3]. The CDM aims to enhance generation efficiency by reducing sampling steps while maintaining high-quality image synthesis. By incorporating consistency constraints, CDM optimizes the training process, mitigating issues such as mode collapse or instability that are often encountered in traditional diffusion models. This makes CDM particularly advantageous in scenarios requiring real-time performance[4]. In addition to diffusion models, approaches such as the Masked Generative Image Transformer (MaskGIT) utilize a masked prediction mechanism to generate images by progressively predicting masked regions of the image. This method reduces computational complexity during the generation process while improving generation efficiency. Certainly, the Visual AutoRegressive (VAR) model is also a viable option. It integrates the Transformer architecture and enhances generation efficiency and quality through "next-scale prediction" . In the field of AR, methods such as the Vector Quantized Generative Adversarial Network (VQGAN), which integrates VQ-VAE and GAN, the Vision Transformer with Vector Quantization (ViTVQ) based on Vision Transformer (ViT), and the large-scale pre-trained LlamaGen-B have significantly enriched the domain of image generation.

However, in the process of progressively generating high-resolution images from low-resolution inputs, the VAR model may exhibit the issue where prediction errors at early scales can be amplified, leading to inconsistencies or distortions in local details of the final image[5]. Although MaskGIT performs well in capturing global structures, local details are prone to distortion when generating high-resolution images. Models such as VQGAN and ViTVQ also suffer from the issue of detail blurring when generating complex scenes. And a limitation of DDPMs and CDM lies in their uniform processing of all pixels

during noise addition or removal, without assigning specialized weights to semantically critical regions. This results in suboptimal preservation of fine-grained details[6]. By introducing explicit modeling of inter-pixel relationships into the DDPM framework, the local structural consistency and detail fidelity of generated images can be substantially enhanced[7]. Embedding a pixel-wise interaction mechanism (for instance, gradient propagation governed by the principles of thermal diffusion) within the diffusion process enables dynamic coordination of signal evolution within local regions at each denoising step, thereby achieving better alignment with the inherent continuity priors of natural images. Such refinement allows the generation process to more accurately capture coherent micro textures (e.g. hair) while mitigating edge blurring or localized artifacts caused by isolated pixel optimization—all achieved without compromising compatibility with the original DDPM training paradigm or introducing additional adversarial training components or architectural complexities.

Section II introduces the diffusion and generation processes of DDPMs. Section III provides a detailed description of the proposed HDM and its modifications to DDPM. Section IV presents experimental results comparing HDM, DDPM, and other models under identical test datasets, and Section V gives the conclusion.

2 RELATED WORK

We briefly introduce the mathematical formulation and procedures of DDPM[8]. Given a data distribution $\mathbf{u}_0 \sim q(\mathbf{u}_0)$, we define a forward noising process q which produces latents \mathbf{u}_1 through \mathbf{u}_T by adding Gaussian noise at time t with variance $\beta_t \in (0,1)$ as follows:

$$q(\mathbf{u}_1, \dots, \mathbf{u}_T | \mathbf{u}_0) = \prod_{t=1}^T q(\mathbf{u}_t | \mathbf{u}_{t-1}) \quad (1)$$

The diffusion process formula for the initial image \mathbf{u}_0 is given by $\mathbf{u}_t = \sqrt{1 - \beta_t} \mathbf{u}_{t-1} + \sqrt{\beta_t} \boldsymbol{\varepsilon}_t$. The noise-adding process can be regarded as multiplying a coefficient based on the previous step and then adding a Gaussian distribution with a mean of 0 and a variance of β_t , thus the noise-adding process is deterministic[9]. In DDPMs, we handcraft the transition kernel $q(\mathbf{u}_t | \mathbf{u}_{t-1})$ to incrementally transform the data distribution $q(\mathbf{u}_0)$ into a tractable prior distribution. It is often written in the following form:

$$q(\mathbf{u}_t | \mathbf{u}_{t-1}) = \mathcal{N}(\mathbf{u}_t; \sqrt{1 - \beta_t} \mathbf{u}_{t-1}, \beta_t \mathbf{I}) \quad (2)$$

If $\alpha_t = 1 - \beta_t$, substituting into the expression for \mathbf{u}_t and iteratively deriving, the formula from \mathbf{u}_0 to \mathbf{u}_t can be obtained:

$$\begin{aligned} \mathbf{u}_t &= \sqrt{1 - \beta_t} \mathbf{u}_{t-1} + \sqrt{\beta_t} \boldsymbol{\varepsilon}_t = \sqrt{\alpha_t} \mathbf{u}_{t-1} + \sqrt{\beta_t} \boldsymbol{\varepsilon}_t \\ &= \sqrt{\alpha_t} (\sqrt{\alpha_{t-1}} \mathbf{u}_{t-2} + \sqrt{\beta_{t-1}} \boldsymbol{\varepsilon}_{t-1}) + \sqrt{\beta_t} \boldsymbol{\varepsilon}_t \\ &= \sqrt{\alpha_t \alpha_{t-1}} \mathbf{u}_{t-2} + \sqrt{\alpha_t \beta_{t-1}} \boldsymbol{\varepsilon}_{t-1} + \sqrt{\beta_t} \boldsymbol{\varepsilon}_t \\ &= \sqrt{\alpha_t \alpha_{t-1}} (\sqrt{\alpha_{t-2}} \mathbf{u}_{t-3} + \sqrt{\beta_{t-2}} \boldsymbol{\varepsilon}_{t-2}) + \sqrt{\alpha_t \beta_{t-1}} \boldsymbol{\varepsilon}_{t-1} + \sqrt{\beta_t} \boldsymbol{\varepsilon}_t \\ &= \sqrt{\alpha_t \alpha_{t-1} \alpha_{t-2}} \mathbf{u}_{t-3} + \sqrt{\alpha_t \alpha_{t-1} \beta_{t-2}} \boldsymbol{\varepsilon}_{t-2} + \sqrt{\alpha_t \beta_{t-1}} \boldsymbol{\varepsilon}_{t-1} + \sqrt{\beta_t} \boldsymbol{\varepsilon}_t \\ &= \sqrt{\alpha_t \alpha_{t-1} \dots \alpha_1} \mathbf{u}_0 + \sqrt{\alpha_t \alpha_{t-1} \dots \alpha_2 \beta_1} \boldsymbol{\varepsilon}_1 + \sqrt{\alpha_t \alpha_{t-1} \dots \alpha_3 \beta_2} \boldsymbol{\varepsilon}_2 + \dots \\ &\quad + \sqrt{\alpha_t \alpha_{t-1} \beta_{t-2}} \boldsymbol{\varepsilon}_{t-2} + \sqrt{\alpha_t \beta_{t-1}} \boldsymbol{\varepsilon}_{t-1} + \sqrt{\beta_t} \boldsymbol{\varepsilon}_t \end{aligned}$$

According to the superposition formula of Gaussian distributions, their sum satisfies a Gaussian distribution with a mean of 0 and a variance equal to the sum of the variances of the individual components.

$$\begin{aligned} &\alpha_t \alpha_{t-1} \dots \alpha_1 + \alpha_t \alpha_{t-1} \dots \alpha_2 \beta_1 + \alpha_t \alpha_{t-1} \dots \alpha_3 \beta_2 + \dots + \alpha_t \beta_{t-1} + \beta_t \\ &= \alpha_t \alpha_{t-1} \dots \alpha_2 (\alpha_1 + \beta_1) + \alpha_t \alpha_{t-1} \dots \alpha_3 \beta_2 + \dots + \alpha_t \alpha_{t-1} \beta_{t-2} + \alpha_t \beta_{t-1} + \beta_t \end{aligned}$$

$$\begin{aligned}
&= \alpha_t \alpha_{t-1} \cdots \alpha_2 \times 1 + \alpha_t \alpha_{t-1} \cdots \alpha_3 \beta_2 + \cdots + \alpha_t \alpha_{t-1} \beta_{t-2} + \alpha_t \beta_{t-1} + \beta_t \\
&= \alpha_t \alpha_{t-1} \cdots \alpha_3 (\alpha_2 + \beta_2) + \cdots + \alpha_t \alpha_{t-1} \beta_{t-2} + \alpha_t \beta_{t-1} + \beta_t \\
&= \alpha_t \alpha_{t-1} \cdots \alpha_3 \times 1 + \cdots + \alpha_t \alpha_{t-1} \beta_{t-2} + \alpha_t \beta_{t-1} + \beta_t \\
&= \cdots \cdots = \alpha_t + \beta_t = 1
\end{aligned}$$

Notably, Sohl-Dickstein et al. (2015) [10] demonstrated that the Gaussian transition kernel enables the marginalization of the joint distribution in Eq. (1), thereby deriving the closed-form expression of $q(\mathbf{u}_t | \mathbf{u}_0)$ across all $t \in \{0, 1, \dots, T\}$. While $\bar{\alpha}_t := \prod_{s=0}^t \alpha_s$, we have

$$q(\mathbf{u}_t | \mathbf{u}_0) = \mathcal{N}(\mathbf{u}_t; \sqrt{\bar{\alpha}_t} \mathbf{u}_0, (1 - \bar{\alpha}_t) \mathbf{I}) \quad (3)$$

The final diffusion formula of DDPM can be expressed as:

$$\mathbf{u}_t = \sqrt{\bar{\alpha}_t} \mathbf{u}_0 + \sqrt{1 - \bar{\alpha}_t} \boldsymbol{\varepsilon}_t \quad (4)$$

When $\bar{\alpha}_T \approx 0$, the distribution of \mathbf{u}_t asymptotically converges to a Gaussian distribution. In simple terms, the forward process adds noise to the data until all structure is destroyed [11]. To generate new data samples, one begins with an unstructured noise vector sampled from the prior distribution and gradually removes noise by running a learnable Markov chain in reverse time [12]. If the exact $q(\mathbf{u}_{t-1} | \mathbf{u}_t)$ is known, we can sample from \mathbf{u}_t and thereby complete the reverse process to obtain $q(\mathbf{u}_0)$. The entire data distribution determines $q(\mathbf{u}_{t-1} | \mathbf{u}_t)$, which is approximated in the following form.

$$p_\theta(\mathbf{u}_{t-1} | \mathbf{u}_t) = \mathcal{N}(\mathbf{u}_{t-1}; \boldsymbol{\mu}_\theta(\mathbf{u}_t, t), \boldsymbol{\Sigma}_\theta(\mathbf{u}_t, t)) \quad (5)$$

where θ denotes model parameters, and $\boldsymbol{\mu}_\theta(\mathbf{u}_t, t)$ and $\boldsymbol{\Sigma}_\theta(\mathbf{u}_t, t)$ represent the mean and variance, respectively. Both the mean and variance are parameterized by the neural network [13]. Thus, we can first sample a noise vector $\mathbf{u}_T \sim p(\mathbf{u}_T)$ to obtain a sample \mathbf{u}_0 , and then iteratively sample from $\mathbf{u}_{t-1} \sim p_\theta(\mathbf{u}_{t-1} | \mathbf{u}_t)$ until $t=1$. We need to train the reverse Markov chain to achieve the effect of time reversal that matches the forward Markov chain, which is the key to the success of this sampling process. In other words, to make the joint distribution $p_\theta(\mathbf{u}_0, \mathbf{u}_1, \dots, \mathbf{u}_T) = p(\mathbf{u}_T) \prod_{t=1}^T p_\theta(\mathbf{u}_{t-1} | \mathbf{u}_t)$ of the reverse Markov chain infinitely close to the forward process $q(\mathbf{u}_0, \mathbf{u}_1, \dots, \mathbf{u}_T) = q(\mathbf{u}_0) \prod_{t=1}^T q(\mathbf{u}_t | \mathbf{u}_{t-1})$ [14], we need to adjust θ . This process is implemented by minimizing the KL divergence between the two:

$$\text{KL}(q(\mathbf{u}_0, \mathbf{u}_1, \dots, \mathbf{u}_T) \parallel p_\theta(\mathbf{u}_0, \mathbf{u}_1, \dots, \mathbf{u}_T)) \quad (6)$$

$$\stackrel{(i)}{=} -\mathbb{E}_{q(\mathbf{u}_0, \mathbf{u}_1, \dots, \mathbf{u}_T)} [\log p_\theta(\mathbf{u}_0, \mathbf{u}_1, \dots, \mathbf{u}_T)] + \text{Const} \quad (7)$$

$$\stackrel{(ii)}{=} \underbrace{\mathbb{E}_{q(\mathbf{u}_0, \mathbf{u}_1, \dots, \mathbf{u}_T)} \left[-\log p(\mathbf{u}_T) - \sum_{t=1}^T \log \frac{p_\theta(\mathbf{u}_{t-1} | \mathbf{u}_t)}{q(\mathbf{u}_t | \mathbf{u}_{t-1})} \right]}_{:= -L_{\text{VLB}}(\mathbf{u}_0)} + \text{Const} \quad (8)$$

$$\stackrel{(iii)}{\geq} \mathbb{E}[-\log p_\theta(\mathbf{u}_0)] + \text{Const} \quad (9)$$

where (i) is from the definition of KL divergence, (ii) is from the fact that $q(\mathbf{u}_0, \mathbf{u}_1, \dots, \mathbf{u}_T)$ and $p_\theta(\mathbf{u}_0, \mathbf{u}_1, \dots, \mathbf{u}_T)$ are both products of distributions, and (iii) is from Jensen's inequality [15]. The first term in Eq.(8) is the variational lower bound (VLB) of the log-likelihood of \mathbf{u}_0 [16], which serves as the objective for training the probabilistic generative model, while const is a constant independent of θ and does not affect the optimization [17]. Maximizing the VLB is the training objective of DDPM, which is a sum of independent terms and thus is straightforward to optimize, alternatively, minimizing the negative VLB can also be performed. The network architecture employed in this study is consistent with that of DDPM, utilizing the U-Net structure.

3 HEAT DIFFUSION MODEL

In this paper, to incorporate the relationships between adjacent pixels into the computation process of DDPM, the discretized heat equation is selected, and the rationale for choosing the heat equation will be explained step-by-step in the subsequent formula derivations.

Given $u = u(x, y, t)$, it expresses the temperature at position (x, y) and time t . For the heat equation, it has the following form:

$$\frac{\partial u}{\partial t} - \kappa \nabla^2 u = 0 \quad (10)$$

where κ denotes the thermal diffusion coefficient and $\nabla^2 = \frac{\partial^2}{\partial x^2} + \frac{\partial^2}{\partial y^2}$ represents the spatial Laplacian operator. The physical essence of the equation lies in its description of energy equilibrium driven by local gradients, i.e., heat diffuses from regions of high gradient to those of low gradient. This is highly similar to the gradients employed in score-based generative models, where gradient-guided learning drives the generated samples to asymptotically approach the true data distribution. We need to discretize it. Take $x = i\Delta$, $y = j\Delta$, $t = n\tau$, the result after discretization is:

$$u_n^{i,j} = u(i\Delta, j\Delta, n\tau)$$

After introducing the superscripts i and j , the adaptability of the discretized modeling becomes more intuitive. Digital images are essentially two-dimensional discrete grids, which are completely isomorphic to the difference grids used in the numerical solution of the heat equation. Therefore, we can regard i and j as the position coordinates of a certain pixel in the image. Performing first-order difference approximation and second-order difference approximation, the following forms are obtained:

$$\frac{\partial u}{\partial t} \Big|_n^{i,j} \approx \frac{u_{n+1}^{i,j} - u_n^{i,j}}{\tau} \quad (\text{First-order forward difference})$$

$$\frac{\partial u}{\partial t} \Big|_{n+1}^{i,j} \approx \frac{u_{n+1}^{i,j} - u_n^{i,j}}{\tau} \quad (\text{First-order backward difference})$$

$$\frac{\partial u}{\partial x} \Big|_n^{i+\frac{1}{2},j} \approx \frac{u_n^{i+1,j} - u_n^{i,j}}{\Delta} \quad (\text{Central difference at } i + \frac{1}{2})$$

$$\frac{\partial u}{\partial x} \Big|_n^{i-\frac{1}{2},j} \approx \frac{u_n^{i,j} - u_n^{i-1,j}}{\Delta} \quad (\text{Central difference at } i - \frac{1}{2})$$

$$\frac{\partial u}{\partial y} \Big|_n^{i,j+\frac{1}{2}} \approx \frac{u_n^{i,j+1} - u_n^{i,j}}{\Delta} \quad (\text{Central difference at } j + \frac{1}{2})$$

$$\frac{\partial u}{\partial y} \Big|_n^{i,j-\frac{1}{2}} \approx \frac{u_n^{i,j} - u_n^{i,j-1}}{\Delta} \quad (\text{Central difference at } j - \frac{1}{2})$$

$$\frac{\partial^2 u}{\partial x^2} \Big|_n^{i,j} \approx \frac{u_n^{i+1,j} - 2u_n^{i,j} + u_n^{i-1,j}}{\Delta^2} \quad (\text{Second-order difference})$$

$$\frac{\partial^2 u}{\partial y^2} \Big|_n^{i,j} \approx \frac{u_n^{i,j+1} - 2u_n^{i,j} + u_n^{i,j-1}}{\Delta^2} \quad (\text{Second-order difference})$$

Applying forward difference to the temporal of the heat equation (10) at $t = n\tau$ yields:

$$u_{n+1}^{i,j} - u_n^{i,j} = K(u_n^{i+1,j} + u_n^{i-1,j} + u_n^{i,j+1} + u_n^{i,j-1} - 4u_n^{i,j})$$

where:

$$K = \frac{\kappa\tau}{\Delta^2}$$

Applying backward difference to the temporal of the heat equation (10) at $t = (n+1)\tau$ yields:

$$u_{n+1}^{i,j} - u_n^{i,j} = K(u_{n+1}^{i+1,j} + u_{n+1}^{i-1,j} + u_{n+1}^{i,j+1} + u_{n+1}^{i,j-1} - 4u_{n+1}^{i,j})$$

A weighted summation of the above two equations yields (where $0 \leq \theta \leq 1$):

$$u_{n+1}^{i,j} - u_n^{i,j} = \theta K(u_n^{i+1,j} + u_n^{i-1,j} + u_n^{i,j+1} + u_n^{i,j-1} - 4u_n^{i,j}) \\ + (1 - \theta)K(u_{n+1}^{i+1,j} + u_{n+1}^{i-1,j} + u_{n+1}^{i,j+1} + u_{n+1}^{i,j-1} - 4u_{n+1}^{i,j})$$

The scheme reduces to fully explicit when $\theta = 1$, fully implicit when $\theta = 0$, and Crank-Nicolson when $\theta = 1/2$ [18]. The above equation can be rearranged as (valid for $0 < i < I - 1$, $0 < j < J - 1$):

$$(1 + 4(1 - \theta)K)u_{n+1}^{i,j} - (1 - \theta)K(u_{n+1}^{i+1,j} + u_{n+1}^{i-1,j} + u_{n+1}^{i,j+1} + u_{n+1}^{i,j-1}) \\ = (1 - 4\theta K)u_n^{i,j} + \theta K(u_n^{i+1,j} + u_n^{i-1,j} + u_n^{i,j+1} + u_n^{i,j-1}) \quad (11)$$

In this way, the positional and quantitative relationship between a certain point and its four adjacent points can be obtained.

However, the given equation fails to determine the values at the positions $i=0$, $I - 1$ and $j=0$, $J - 1$, and its adverse effects cannot be predicted a priori; therefore, an appropriate boundary condition should be selected. A common boundary condition involves specifying fixed values at the boundaries. Here, the boundary conditions are assumed to be 0.

To avoid affecting the subsequent reasoning process due to the complexity of the formulas, we introduce the matrix form, arranging $u_n^{i,j}$ as a column vector ($0 \leq i \leq I - 1$, $0 \leq j \leq J - 1$), for ease of calculation, the values of I and J here directly represent the number of rows and columns of the image dimensions, and obtain:

$$\mathbf{u}_n = \begin{bmatrix} u_n^{0,0} \\ \vdots \\ u_n^{0,J-1} \\ \vdots \\ u_n^{I-1,0} \\ \vdots \\ u_n^{I-1,J-1} \end{bmatrix}$$

At this point, Eq. (11) is written in matrix form:

$$\mathbf{S}\mathbf{u}_{n+1} = \mathbf{T}\mathbf{u}_n$$

Matrix \mathbf{S} and \mathbf{T} can be derived in the following form (fixed boundary):

$$\mathbf{S} = \begin{bmatrix} 1 + 4(1 - \theta)K & (\theta - 1)K & 0 & \dots & (\theta - 1)K & \dots & 0 \\ 0 & 1 + 4(1 - \theta)K & (\theta - 1)K & 0 & 0 & \ddots & 0 \\ 0 & 0 & 1 + 4(1 - \theta)K & (\theta - 1)K & \ddots & 0 & (\theta - 1)K \\ \vdots & \vdots & \vdots & \ddots & \ddots & \ddots & \vdots \\ (\theta - 1)K & 0 & 0 & 0 & 1 + 4(1 - \theta)K & (\theta - 1)K & 0 \\ \vdots & \ddots & 0 & \ddots & 0 & 1 + 4(1 - \theta)K & (\theta - 1)K \\ 0 & 0 & (\theta - 1)K & \dots & 0 & 0 & 1 + 4(1 - \theta)K \end{bmatrix}$$

$$\mathbf{T} = \begin{bmatrix} 1 - 4\theta K & \theta K & 0 & \dots & \theta K & \dots & 0 \\ 0 & 1 - 4\theta K & \theta K & 0 & 0 & \ddots & 0 \\ 0 & 0 & 1 - 4\theta K & \theta K & \ddots & 0 & \theta K \\ \vdots & \vdots & \vdots & \ddots & \ddots & 0 & \vdots \\ \theta K & 0 & 0 & 0 & 1 - 4\theta K & \theta K & 0 \\ \vdots & \ddots & 0 & \ddots & 0 & 1 - 4\theta K & \theta K \\ 0 & 0 & \theta K & \dots & 0 & 0 & 1 - 4\theta K \end{bmatrix}$$

This is not accurate because, in real images, the values of boundary pixels may vary with the content. Fixing the boundary values could lead to unnatural transitions or artifacts in the boundary regions of the generated images. This approach is discouraged because it impedes the natural outward propagation of the diffusion process, resulting in truncation artifacts at the boundary regions. The consequence of this approach is that all values of u ultimately converge to fixed constants as thermal diffusion progresses. Therefore, whether the boundary value is zero or non-zero constant, they must affect the overall heat exchange of the system.

The boundary condition used here is adiabatic condition:

$$\frac{\partial u}{\partial x}\Big|_n^{0,j} = \frac{\partial u}{\partial x}\Big|_n^{I-1,j} = \frac{\partial u}{\partial y}\Big|_n^{i,0} = \frac{\partial u}{\partial y}\Big|_n^{i,J-1} = 0$$

Taking the boundary at $i = 0$, $1 < j < J - 1$ as an example, the discrete form of $\frac{\partial u}{\partial x}\Big|_n^{0,j} = 0$ is obtained:

$$\frac{u_n^{1,j} - u_n^{-1,j}}{2\Delta} = 0$$

This yields the relation $u_n^{-1,j} = u_n^{1,j}$, which when substituted into Eq. (11) leads to the following form:

$$\begin{aligned} (1 + 4(1-\theta)K)u_{n+1}^{0,j} - (1 - \theta)K(2u_n^{1,j} + u_{n+1}^{0,j+1} + u_{n+1}^{0,j-1}) \\ = (1 - 4\theta K)u_n^{0,j} + \theta K(2u_n^{1,j} + u_n^{0,j+1} + u_n^{0,j-1}) \end{aligned}$$

This condition ensures smooth transitions at the image boundaries, preventing the introduction of external information. The adiabatic condition simplifies the numerical implementation of the boundary conditions, reduces computational complexity, and is well-suited for image inpainting and generation tasks. To better illustrate the form of the boundary conditions, the matrix \mathbf{S} and \mathbf{T} corresponding to $I=3$, $J=3$ is explicitly expressed as follows:

$$\mathbf{S} = \begin{bmatrix} 1+4(1-\theta)K & 2(\theta-1)K & 0 & 2(\theta-1)K & 0 & 0 & 0 & 0 & 0 \\ (\theta-1)K & 1+4(1-\theta)K & (\theta-1)K & 0 & 2(\theta-1)K & 0 & 0 & 0 & 0 \\ 0 & 2(\theta-1)K & 1+4(1-\theta)K & 0 & 0 & 2(\theta-1)K & 0 & 0 & 0 \\ (\theta-1)K & 0 & 0 & 1+4(1-\theta)K & 2(\theta-1)K & 0 & (\theta-1)K & 0 & 0 \\ 0 & (\theta-1)K & 0 & (\theta-1)K & 1+4(1-\theta)K & (\theta-1)K & 0 & (\theta-1)K & 0 \\ 0 & 0 & (\theta-1)K & 0 & 2(\theta-1)K & 1+4(1-\theta)K & 0 & 0 & (\theta-1)K \\ 0 & 0 & 0 & 2(\theta-1)K & 0 & 0 & 1+4(1-\theta)K & 2(\theta-1)K & 0 \\ 0 & 0 & 0 & 0 & 2(\theta-1)K & 0 & (\theta-1)K & 1+4(1-\theta)K & (\theta-1)K \\ 0 & 0 & 0 & 0 & 0 & 2(\theta-1)K & 0 & 2(\theta-1)K & 1+4(1-\theta)K \end{bmatrix}$$

$$\mathbf{T} = \begin{bmatrix} 1-4\theta K & 2\theta K & 0 & 2\theta K & 0 & 0 & 0 & 0 & 0 \\ \theta K & 1-4\theta K & \theta K & 0 & 2\theta K & 0 & 0 & 0 & 0 \\ 0 & 2\theta K & 1-4\theta K & 0 & 0 & 2\theta K & 0 & 0 & 0 \\ \theta K & 0 & 0 & 1-4\theta K & 2\theta K & 0 & \theta K & 0 & 0 \\ 0 & \theta K & 0 & \theta K & 1-4\theta K & \theta K & 0 & \theta K & 0 \\ 0 & 0 & \theta K & 0 & 2\theta K & 1-4\theta K & 0 & 0 & \theta K \\ 0 & 0 & 0 & 2\theta K & 0 & 0 & 1-4\theta K & 2\theta K & 0 \\ 0 & 0 & 0 & 0 & 2\theta K & 0 & \theta K & 1-4\theta K & \theta K \\ 0 & 0 & 0 & 0 & 0 & 2\theta K & 0 & 2\theta K & 1-4\theta K \end{bmatrix}$$

From $\mathbf{S}\mathbf{u}_{n+1} = \mathbf{T}\mathbf{u}_n$, we can define $\mathbf{A} = \mathbf{S}^{-1}\mathbf{T}$, thereby achieving:

$$\mathbf{u}_{n+1} = \mathbf{A}\mathbf{u}_n$$

Once the matrix representing the positional and quantitative relationships between pixels is obtained, modifications to the diffusion process formula of DDPM can be initiated.

Initially, the diffusion formula can be expressed as:

$$\mathbf{u}_n = \sqrt{\alpha_n}\mathbf{A}\mathbf{u}_{n-1} + \sqrt{1-\alpha_n}\boldsymbol{\varepsilon}_{n-1}, \quad \boldsymbol{\varepsilon}_n \sim \mathcal{N}(0, \mathbf{I}), \quad n = 0 \sim N$$

at this stage, matrix \mathbf{A} is simply embedded into the formula, and in the subsequent derivation process, matrix \mathbf{A} will impose substantial computational complexity. Not only that, but the appearance of \mathbf{A}^n in subsequent calculations will result in the variance of the entire distribution no longer being equal to 1[19]. Maintaining a total variance of 1 ensures that the noise addition in the diffusion process remains controllable, preventing instability or convergence difficulties in the training process caused by excessively large or small variances[20]. A variance of 1 provides a standardized noise scale, enabling the model to learn the data distribution more stably[21]. The generative process of DDPM is the inverse of the diffusion process. If the variance in the diffusion process deviates from 1, the generative process will struggle to accurately reverse the noise-adding steps, leading to a degradation in the quality of the generated outputs[22]. And the natural images typically exhibit local smoothness and continuity, and the

noise-adding process with a variance of 1 can better align with such prior knowledge, thereby preserving the structure and details of the images during the generation process[23]. It is calculated that the matrix \mathbf{A} is invertible. We can derive a matrix \mathbf{A}^{n-N} , thereby enabling the diffusion equation to be expressed in the following form:

$$\mathbf{u}_n = \sqrt{\alpha_n} \mathbf{A} \mathbf{u}_{n-1} + \sqrt{1 - \alpha_n} \mathbf{A}^{n-N} \boldsymbol{\varepsilon}_{n-1}, \quad \boldsymbol{\varepsilon}_n \sim \mathcal{N}(\mathbf{0}, \mathbf{I}) \quad (12)$$

N is the number of time steps and $0 < \alpha_n < 1$. Finally, by performing the same operations on the equations as described in Section 2, we can obtain:

$$\mathbf{u}_n = \sqrt{\bar{\alpha}_n} \mathbf{A}^n \mathbf{u}_0 + \mathbf{A}^{n-N} \mathbf{e}'_n \quad (13)$$

where $\mathbf{e}'_n = \sqrt{\alpha_n \cdots \alpha_2 (1 - \alpha_1)} \boldsymbol{\varepsilon}_0 + \sqrt{\alpha_n \cdots \alpha_3 (1 - \alpha_2)} \boldsymbol{\varepsilon}_1 + \cdots + \sqrt{\alpha_n (1 - \alpha_{n-1})} \boldsymbol{\varepsilon}_{n-2} + \sqrt{1 - \alpha_n} \boldsymbol{\varepsilon}_{n-1}$,

$\mathbf{e}'_n \sim \mathcal{N}(\mathbf{0}, (1 - \bar{\alpha}_n) \mathbf{I})$. Rearranging the equation yields: $\mathbf{u}_n = \sqrt{\bar{\alpha}_n} \mathbf{A}^n \mathbf{u}_0 + \sqrt{1 - \bar{\alpha}_n} \mathbf{A}^{n-N} \mathbf{e}_n$,

$\mathbf{e}_n \sim \mathcal{N}(\mathbf{0}, \mathbf{I})$. To simplify the equation and facilitate an intuitive understanding of its variations, we have:

$$\mathbf{u}_N = \sqrt{\bar{\alpha}_N} \mathbf{A}^N \mathbf{u}_0 + \sqrt{1 - \bar{\alpha}_N} \mathbf{e}_N \quad (14)$$

when N is sufficiently large, $\bar{\alpha}_N = \alpha_N \cdots \alpha_1 \rightarrow 0$, then $\mathbf{u}_N \rightarrow \mathbf{e}_N \sim \mathcal{N}(\mathbf{0}, \mathbf{I})$. Based on Equation (12) and Equation (14), the forward transition probability of the noise-adding process can be derived as follows:

$$\begin{aligned} q(\mathbf{u}_n | \mathbf{u}_{n-1}) &= \mathcal{N}(\mathbf{u}_n | \sqrt{\alpha_n} \mathbf{A} \mathbf{u}_{n-1}, (1 - \alpha_n) \mathbf{B}_n) \\ q(\mathbf{u}_n | \mathbf{u}_0) &= \mathcal{N}(\mathbf{u}_n | \sqrt{\bar{\alpha}_n} \mathbf{A}^n \mathbf{u}_0, (1 - \bar{\alpha}_n) \mathbf{B}_n) \end{aligned}$$

where $\mathbf{B}_n = \mathbf{A}^{n-N} (\mathbf{A}^{n-N})^T$ (Matrix \mathbf{B} is evidently symmetric).

The backward transition probability of the diffusion process is:

$$\begin{aligned} q(\mathbf{u}_{n-1} | \mathbf{u}_n, \mathbf{u}_0) &= \frac{q(\mathbf{u}_n | \mathbf{u}_{n-1}) q(\mathbf{u}_{n-1} | \mathbf{u}_0)}{q(\mathbf{u}_n | \mathbf{u}_0)} = \\ &= \frac{N(\mathbf{u}_n | \sqrt{\alpha_n} \mathbf{A} \mathbf{u}_{n-1}, (1 - \alpha_n) \mathbf{B}_n) N(\mathbf{u}_{n-1} | \sqrt{\bar{\alpha}_{n-1}} \mathbf{A}^{n-1} \mathbf{u}_0, (1 - \bar{\alpha}_{n-1}) \mathbf{B}_{n-1})}{N(\mathbf{u}_n | \sqrt{\bar{\alpha}_n} \mathbf{A}^n \mathbf{u}_0, (1 - \bar{\alpha}_n) \mathbf{B}_n)} \end{aligned}$$

the exponential term is a quadratic form in \mathbf{u}_{n-1} (clearly, the above expression remains a Gaussian function), and the part involving only \mathbf{u}_{n-1} is written as:

$$\begin{aligned} &\propto \exp \left\{ -\frac{1}{2} \left[(\mathbf{u}_n - \sqrt{\alpha_n} \mathbf{A} \mathbf{u}_{n-1})^T (1 - \alpha_n)^{-1} \mathbf{B}_n^{-1} (\mathbf{u}_n - \sqrt{\alpha_n} \mathbf{A} \mathbf{u}_{n-1}) \right. \right. \\ &\quad \left. \left. + (\mathbf{u}_{n-1} - \sqrt{\bar{\alpha}_{n-1}} \mathbf{A}^{n-1} \mathbf{u}_0)^T (1 - \bar{\alpha}_{n-1})^{-1} \mathbf{B}_{n-1}^{-1} (\mathbf{u}_{n-1} - \sqrt{\bar{\alpha}_{n-1}} \mathbf{A}^{n-1} \mathbf{u}_0) \right] \right\} \end{aligned}$$

From the quadratic term in \mathbf{u}_{n-1} in this expression, the covariance matrix of the backward transition probability $q(\mathbf{u}_{n-1} | \mathbf{u}_n, \mathbf{u}_0)$ can be derived:

$$\boldsymbol{\Sigma}_n = [(1 - \alpha_n)^{-1} \alpha_n \mathbf{A}^T \mathbf{B}_n^{-1} \mathbf{A} + (1 - \bar{\alpha}_{n-1})^{-1} \mathbf{B}_{n-1}^{-1}]^{-1}$$

By setting the gradients of the quadratic and linear terms with respect to \mathbf{u}_{n-1} to zero:

$$\begin{aligned} &2(1 - \alpha_n)^{-1} \alpha_n \mathbf{A}^T \mathbf{B}_n^{-1} \mathbf{A} \mathbf{u}_{n-1} + 2(1 - \bar{\alpha}_{n-1})^{-1} \mathbf{B}_{n-1}^{-1} \mathbf{u}_{n-1} - (1 - \alpha_n)^{-1} \sqrt{\alpha_n} \mathbf{A}^T \mathbf{B}_n^{-1} \mathbf{u}_n \\ &\quad - (1 - \alpha_n)^{-1} \sqrt{\alpha_n} \mathbf{A}^T \mathbf{B}_n^{-1} \mathbf{u}_n - (1 - \bar{\alpha}_{n-1})^{-1} \sqrt{\bar{\alpha}_{n-1}} \mathbf{B}_{n-1}^{-1} \mathbf{A}^{n-1} \mathbf{u}_0 \\ &\quad - (1 - \bar{\alpha}_{n-1})^{-1} \sqrt{\bar{\alpha}_{n-1}} \mathbf{B}_{n-1}^{-1} \mathbf{A}^{n-1} \mathbf{u}_0 = 0 \end{aligned}$$

the mean of the backward transition probability $q(\mathbf{u}_{n-1} | \mathbf{u}_n, \mathbf{u}_0)$ can be obtained:

$$\begin{aligned} \boldsymbol{\mu}_n(\mathbf{u}_n, \mathbf{u}_0) &= [(1 - \alpha_n)^{-1} \alpha_n \mathbf{A}^T \mathbf{B}_n^{-1} \mathbf{A} + (1 - \bar{\alpha}_{n-1})^{-1} \mathbf{B}_{n-1}^{-1}]^{-1} [(1 - \alpha_n)^{-1} \sqrt{\alpha_n} \mathbf{A}^T \mathbf{B}_n^{-1} \mathbf{u}_n + \\ &\quad (1 - \bar{\alpha}_{n-1})^{-1} \sqrt{\bar{\alpha}_{n-1}} \mathbf{B}_{n-1}^{-1} \mathbf{A}^{n-1} \mathbf{u}_0] \end{aligned} \quad (15)$$

That is:

$$q(\mathbf{u}_{n-1} | \mathbf{u}_n, \mathbf{u}_0) = \mathcal{N}(\mathbf{u}_{n-1} | \boldsymbol{\mu}_n(\mathbf{u}_n, \mathbf{u}_0), \boldsymbol{\Sigma}_n) \quad (16)$$

While $n = 1$:

$$q(\mathbf{u}'_0|\mathbf{u}_1, \mathbf{u}_0) = \delta(\mathbf{u}'_0 - \mathbf{u}_0)$$

At this point, the formulas for the diffusion process have been fully updated.

The transition probability of the generative process (based on Eq. (16), where θ is a training parameter):

$$p_\theta(\mathbf{u}_{n-1}|\mathbf{u}_n) = \begin{cases} \mathcal{N}(\mathbf{u}_{n-1}|\hat{\boldsymbol{\mu}}_\theta(\mathbf{u}_n), \boldsymbol{\Sigma}_n), n > 1 \\ \mathcal{N}(\mathbf{u}_0|\hat{\boldsymbol{\mu}}_\theta(\mathbf{u}_1), \mathbf{I}), n = 1 \end{cases} \quad (17)$$

Rewrite $\mathbf{u}_n = \sqrt{\bar{\alpha}_n}\mathbf{A}^n\mathbf{u}_0 + \sqrt{1 - \bar{\alpha}_n}\mathbf{A}^{n-N}\mathbf{e}_n$ as $\mathbf{u}_0 = \frac{1}{\sqrt{\bar{\alpha}_n}}(\mathbf{A}^{-n}\mathbf{u}_n - \sqrt{1 - \bar{\alpha}_n}\mathbf{A}^{-N}\mathbf{e}_n)$. Substituting it into Eq.(16) yields:

$$\boldsymbol{\mu}_n(\mathbf{u}_n, \mathbf{u}_0) = \mathbf{C}_n\mathbf{u}_n + \mathbf{D}_n\mathbf{e}_n \quad (18)$$

where:

$$\mathbf{C}_n = \left[(1 - \alpha_n)^{-1}\alpha_n\mathbf{A}^T\mathbf{B}_n^{-1}\mathbf{A} + (1 - \bar{\alpha}_{n-1})^{-1}\mathbf{B}_{n-1}^{-1} \right]^{-1} \left[\frac{\sqrt{\alpha_n}}{1 - \alpha_n}\mathbf{A}^T\mathbf{B}_n^{-1} + \frac{1}{(1 - \bar{\alpha}_{n-1})\sqrt{\alpha_n}}\mathbf{B}_{n-1}^{-1}\mathbf{A}^{-1} \right]$$

$$\mathbf{D}_n = -\frac{\sqrt{1 - \bar{\alpha}_n}}{(1 - \bar{\alpha}_{n-1})\sqrt{\alpha_n}} \left[(1 - \alpha_n)^{-1}\alpha_n\mathbf{A}^T\mathbf{B}_n^{-1}\mathbf{A} + (1 - \bar{\alpha}_{n-1})^{-1}\mathbf{B}_{n-1}^{-1} \right]^{-1} \mathbf{B}_{n-1}^{-1}\mathbf{A}^{n-N-1}$$

According to $\boldsymbol{\mu}_1(\mathbf{u}_1, \mathbf{u}_0) = \mathbf{u}_0$ and $\mathbf{u}_0 = \frac{1}{\sqrt{\bar{\alpha}_n}}(\mathbf{A}^{-n}\mathbf{u}_n - \sqrt{1 - \bar{\alpha}_n}\mathbf{A}^{-N}\mathbf{e}_n)$, when $n = 1$:

$$\mathbf{u}_0 = \boldsymbol{\mu}_1(\mathbf{u}_1, \mathbf{u}_0) = \mathbf{C}_1\mathbf{u}_1 + \mathbf{D}_1\mathbf{e}_1$$

where $\mathbf{C}_1 = \frac{1}{\sqrt{\alpha_1}}\mathbf{A}^{-1}$, $\mathbf{D}_1 = -\sqrt{\frac{1 - \alpha_1}{\alpha_1}}\mathbf{A}^{-N}$. Following the form of Eq. (18), we can obtain:

$$\hat{\boldsymbol{\mu}}_\theta(\mathbf{u}_n) = \mathbf{C}_n\mathbf{u}_n + \mathbf{D}_n\hat{\mathbf{e}}_\theta(\mathbf{u}_n) \quad (19)$$

Now, we have derived the corresponding formulas for both the diffusion process and the generative process of DDPM when incorporating inter-pixel relationships.

We need to employ the ELBO to optimize the objective and identify the distribution that most closely approximates the true distribution[24].

$$\text{ELBO}_\theta(\mathbf{u}_0) = E_{q(\mathbf{u}_1|\mathbf{u}_0)}[\ln p_\theta(\mathbf{u}_0|\mathbf{u}_1)] - \text{D}_{\text{KL}}(q(\mathbf{u}_N|\mathbf{u}_0)||p(\mathbf{u}_N))$$

$$- \sum_{n=2}^N E_{q(\mathbf{u}_n|\mathbf{u}_0)}[\text{D}_{\text{KL}}(q(\mathbf{u}_{n-1}|\mathbf{u}_n, \mathbf{u}_0)||p_\theta(\mathbf{u}_{n-1}|\mathbf{u}_n))]$$

where, based on Eq.(16),Eq.(17),Eq.(18) and Eq.(19), the KL divergence can be derived as follows:

$$\text{D}_{\text{KL}}(q(\mathbf{u}_{n-1}|\mathbf{u}_n, \mathbf{u}_0)||p_\theta(\mathbf{u}_{n-1}|\mathbf{u}_n))$$

$$= \frac{1}{2}[(\boldsymbol{\mu}_n(\mathbf{u}_n, \mathbf{u}_0) - \hat{\boldsymbol{\mu}}_\theta(\mathbf{u}_n))^T \boldsymbol{\Sigma}_n^{-1}(\boldsymbol{\mu}_n(\mathbf{u}_n, \mathbf{u}_0) - \hat{\boldsymbol{\mu}}_\theta(\mathbf{u}_n))]$$

$$= \frac{1}{2}[(\mathbf{e}_n - \hat{\mathbf{e}}_\theta(\mathbf{u}_n))^T \mathbf{D}_n^T \boldsymbol{\Sigma}_n^{-1} \mathbf{D}_n (\mathbf{e}_n - \hat{\mathbf{e}}_\theta(\mathbf{u}_n))]$$

thus, we have:

$$\text{ELBO}_\theta(\mathbf{u}_0) = E_{q(\mathbf{u}_1|\mathbf{u}_0)}[\ln p_\theta(\mathbf{u}_0|\mathbf{u}_1)] - \frac{1}{2} \sum_{n=2}^N E_{q(\mathbf{u}_n|\mathbf{u}_0)} \left[(\mathbf{e}_n - \hat{\mathbf{e}}_\theta(\mathbf{u}_n))^T \mathbf{D}_n^T \boldsymbol{\Sigma}_n^{-1} \mathbf{D}_n (\mathbf{e}_n - \hat{\mathbf{e}}_\theta(\mathbf{u}_n)) \right] + \text{Const} \quad (20)$$

based on Eq.(17), Eq.(19) and $\mathbf{u}_0 = \boldsymbol{\mu}_1(\mathbf{u}_1, \mathbf{u}_0) = \mathbf{C}_1\mathbf{u}_1 + \mathbf{D}_1\mathbf{e}_1$, it can be concluded that(where $\boldsymbol{\Sigma}_1 = \mathbf{I}$):

$$\ln p_\theta(\mathbf{u}_0|\mathbf{u}_1) = -\frac{1}{2}[(\mathbf{u}_0 - \hat{\boldsymbol{\mu}}_\theta(\mathbf{u}_1))^T \boldsymbol{\Sigma}_1^{-1}(\mathbf{u}_0 - \hat{\boldsymbol{\mu}}_\theta(\mathbf{u}_1))] + \text{Const}$$

$$= -\frac{1}{2}[(\mathbf{u}_0 - \mathbf{C}_1\mathbf{u}_1 - \mathbf{D}_1\hat{\mathbf{e}}_\theta(\mathbf{u}_1))^T \boldsymbol{\Sigma}_1^{-1}(\mathbf{u}_0 - \mathbf{C}_1\mathbf{u}_1 - \mathbf{D}_1\hat{\mathbf{e}}_\theta(\mathbf{u}_1))] + \text{Const}$$

$$\begin{aligned}
&= -\frac{1}{2} \left[(\mathbf{D}_1 \mathbf{e}_1 - \mathbf{D}_1 \hat{\mathbf{e}}_\theta(\mathbf{u}_1))^T \boldsymbol{\Sigma}_1^{-1} (\mathbf{D}_1 \mathbf{e}_1 - \mathbf{D}_1 \hat{\mathbf{e}}_\theta(\mathbf{u}_1)) \right] + \text{Const} \\
&= -\frac{1}{2} \left[(\mathbf{e}_1 - \hat{\mathbf{e}}_\theta(\mathbf{u}_1))^T \mathbf{D}_1^T \boldsymbol{\Sigma}_1^{-1} \mathbf{D}_1 (\mathbf{e}_1 - \hat{\mathbf{e}}_\theta(\mathbf{u}_1)) \right] + \text{Const}
\end{aligned}$$

from this, the final ELBO can be calculated as:

$$\text{ELBO}_\theta(\mathbf{u}_0) = -\frac{1}{2} \sum_{n=1}^N E_{q(\mathbf{u}_n|\mathbf{u}_0)} \left[(\mathbf{e}_n - \hat{\mathbf{e}}_\theta(\mathbf{u}_n))^T \mathbf{D}_n^T \boldsymbol{\Sigma}_n^{-1} \mathbf{D}_n (\mathbf{e}_n - \hat{\mathbf{e}}_\theta(\mathbf{u}_n)) \right] + \text{Const}$$

The following two tables respectively outline the program execution sequence of the diffusion process and the generation process.

Algorithm 1 Training

- 1: Receive \mathbf{u}_0 from training data
- 2: **while** not converged do
- 3: Sample $n \sim \mathcal{U}(1, N)$
- 4: Sample $\mathbf{e}_n \sim \mathcal{N}(0, \mathbf{I})$
- 5: Compute $\mathbf{u}_n = \sqrt{\bar{\alpha}_n} \mathbf{A}^n \mathbf{u}_0 + \sqrt{1 - \bar{\alpha}_n} \mathbf{A}^{n-N} \mathbf{e}_n$
- 6: Update $\theta \leftarrow \theta - \eta \nabla_\theta \left[(\mathbf{e}_n - \hat{\mathbf{e}}_\theta(\mathbf{u}_n))^T \mathbf{D}_n^T \boldsymbol{\Sigma}_n^{-1} \mathbf{D}_n (\mathbf{e}_n - \hat{\mathbf{e}}_\theta(\mathbf{u}_n)) \right]$
- 7: **end while**
- 8: return θ

Algorithm 2 Sampling

- 1: Sample $\mathbf{u}_N \sim \mathcal{N}(0, \mathbf{I})$
 - 2: **For** $n = N \sim 1$
 - 3: Sample $\mathbf{z}_n \sim \mathcal{N}(0, \mathbf{I})$
 - 4: Cholesky decomposition $\boldsymbol{\Sigma}_n = \mathbf{L}_n \mathbf{L}_n^T$
 - 5: Compute $\mathbf{u}_{n-1} = \mathbf{C}_n \mathbf{u}_n + \mathbf{D}_n \hat{\mathbf{e}}_\theta(\mathbf{u}_n) + \mathbf{L}_n \mathbf{z}_n$
 - 6: **end for**
 - 7: return u_0
-

It is necessary to supplement some knowledge regarding the selection of the heat equation parameter K as it influences the parameter values in subsequent experiments. The d-dimensional Fourier transform is given by:

$$\frac{1}{(2\pi)^{d/2} (\det \boldsymbol{\Sigma})^{1/2}} \exp \left[-\frac{1}{2} (\mathbf{x} - \boldsymbol{\mu})^T \boldsymbol{\Sigma}^{-1} (\mathbf{x} - \boldsymbol{\mu}) \right] \xrightarrow{\text{FT}} \exp \left[-\frac{1}{2} \boldsymbol{\omega}^T \boldsymbol{\Sigma} \boldsymbol{\omega} - j \boldsymbol{\mu}^T \boldsymbol{\omega} \right]$$

if $\boldsymbol{\Sigma} = \sigma^2 \mathbf{I}$, then:

$$\frac{1}{(2\pi)^{d/2} \sigma^d} \exp \left(-\frac{1}{2\sigma^2} \|\mathbf{x} - \boldsymbol{\mu}\|^2 \right) \xrightarrow{\text{FT}} \exp \left(-\frac{\sigma^2}{2} \|\boldsymbol{\omega}\|^2 - j \boldsymbol{\mu}^T \boldsymbol{\omega} \right) \quad (21)$$

For the initial value problem:

$$\begin{cases} \frac{\partial u}{\partial t} - \kappa \nabla^2 u = 0 \\ u(\mathbf{x}, 0) = u_0(\mathbf{x}) \end{cases}$$

assuming $U(\boldsymbol{\omega}, t)$ is the Fourier transform of $u(\mathbf{x}, t)$ with respect to \mathbf{x} , and $U_0(\boldsymbol{\omega})$ is the Fourier transform of $u_0(\mathbf{x})$, then:

$$\frac{\partial U}{\partial t} + \kappa \|\boldsymbol{\omega}\|^2 U = 0$$

its solution is:

$$U = \begin{cases} U_0 \exp[-\kappa \|\boldsymbol{\omega}\|^2 t], & t > 0 \\ 0, & t \leq 0 \end{cases}$$

by setting $\sigma = \sqrt{2\kappa t}$, the following can be derived from Eq. (21):

$$\frac{1}{(4\pi\kappa t)^{d/2}} \exp\left(-\frac{1}{4\kappa t} \|\mathbf{x}\|^2\right) \xrightarrow{\text{FT}} \exp(-\kappa t \|\boldsymbol{\omega}\|^2)$$

According to the properties of the Fourier transform, the inverse Fourier transform of the product of two functions is the convolution of their respective inverse Fourier transforms:

$$u(\mathbf{x}, t) = \begin{cases} \int G(\mathbf{x} - \mathbf{x}', t) U_0(\mathbf{x}') d\mathbf{x}', & t > 0 \\ 0, & t \leq 0 \end{cases}$$

where:

$$G(\mathbf{x}, t) = \frac{1}{(4\pi\kappa t)^{d/2}} \exp\left(-\frac{1}{4\kappa t} \|\mathbf{x}\|^2\right)$$

By setting $U_0(\mathbf{x}) = \delta(\mathbf{x})$, we obtain $u(\mathbf{x}, t) = G(\mathbf{x}, t)$. By fixing \mathbf{x} , the curve of $G(\mathbf{x}, t)$ with respect to t is as shown in Figure 1:

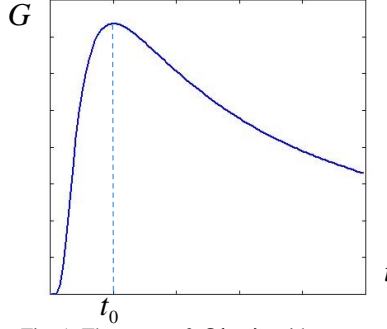


Fig. 1. The curve of $G(\mathbf{x}, t)$ with respect to t

The peak time can be determined as:

$$t_0 = \frac{\|\mathbf{x}\|^2}{2d\kappa}$$

By setting $t_0 = \tau$, $\mathbf{x} = (\gamma\Delta, 0, \dots, 0)$, which implies that heat propagates γ grid points over one time step, the above equation can be written as

$$K = \frac{\kappa\tau}{\Delta^2} = \frac{\gamma^2}{2d}$$

When $d=2$, γ is chosen to satisfy $\gamma < 1/\sqrt{2}$, for example, $\gamma = 0.5$. It should be noted that the Crank-Nicolson scheme is unconditionally stable, imposing no restrictions on parameter K . However, matrix A is invertible, requiring $K < \frac{1}{2d}$ [18].

4 EXPERIMENTAL RESULTS

4.1 Dataset Preparation.

The dataset utilized in this experiment consists of 500 images with a resolution of 64×64 from CIFAR-10, of which 400 images were used as the training set and 100 images as the test set. From the LSUN

dataset, 500 images with a resolution of 256×256 were selected from the "bridge" category, and another 500 images with the same resolution were selected from the "church" category. For both categories, 400 images were used as the training set and 100 images as the test set. Finally, 1000 images with a resolution of 256×256 were selected from the ImageNet dataset, of which 800 images were used as the training set and 200 images as the test set.

4.2 Experimental Configuration.

The training for this experiment was conducted on a computer equipped with 16GB of memory and an RTX 2080Ti GPU, utilizing Python version 3.9.13 and the deep learning framework PyTorch version 1.13.1.

4.3 Experimental Procedure and Results.

In this section, we demonstrate that, under the same number of iterations as DDPM, HDM generates images of higher quality, with FID scores reduced by 0.1 points on CIFAR-10. HDM demonstrates superior performance with a 3.0 point reduction in FID on 256×256 LSUN dataset and a 4.2 point FID improvement on 256×256 ImageNet dataset. To ensure that the number of neural network evaluations required during sampling matches that of previous work, we set $N=1000$ for all experiments. Except for the value of K , the selection of hyperparameters is consistent with those specified in the original DDPM paper.

The criteria selected for evaluating the quality of images generated by the model are FID and IS. FID utilizes a pre-trained Inception-v3 network to extract features from both generated and real images, measuring the discrepancy between the distributions of generated and real images. Its calculation formula is as follows:

$$FID(X, Y) = \|\mu_X - \mu_Y\|^2 + Tr(\Sigma_X + \Sigma_Y - 2(\Sigma_X \Sigma_Y)^{1/2})$$

where X is the feature set of the generated images, $X = \{x_1, x_2, \dots, x_m\}$ and $x_i \in \mathbb{R}^d$ is the feature vector of the i -th generated image (with d being the feature dimension of Inception-v3). Y is the feature set of the real images, where y_j is the feature vector of the j real image. μ_X is the mean vector of the generated image features, μ_Y is the mean vector of the real image features, Σ_X is the covariance matrix of the generated image features, and Σ_Y is the covariance matrix of the real image features.

IS is used to measure the diversity and clarity of generated images, and its calculation formula is as follows:

$$IS(X) = \exp(E_{x \sim X}[KL(p(y|x) \parallel p(y))])$$

where X is the set of generated images, and x_i is the i -th generated image. $p(y|x)$ is the class probability distribution output by the Inception-v3 network given the image x , and $p(y)$ is the marginal class probability distribution.

$$p(y) = \frac{1}{m} \sum_{i=1}^m p(y|x_i)$$

To determine the value of θ and K in the matrix, we conducted training on 64×64 images from the CIFAR-10 dataset. Figure 2 illustrates the variation in FID scores of generated images with respect to changes in K and θ values, where all FID scores were obtained with a sampling step count of 1000.

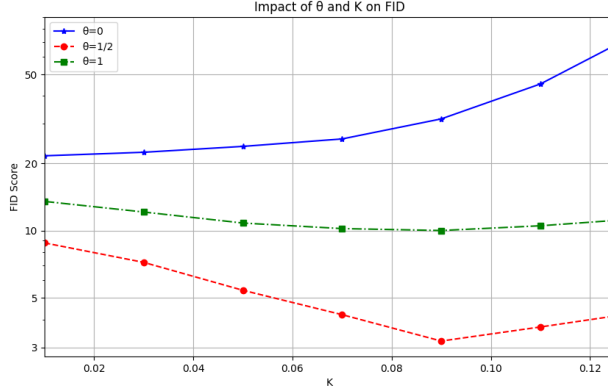


Fig. 2: The impact of θ and K on the FID score.

For 0 sampling steps, the FID score is practically meaningless. At 1000 sampling steps, all three FID scores are below 50; thus, the vertical axis is simply set to 50 for zero sampling steps. The figure demonstrates that when $\theta = 1/2$, the unconditionally stable scheme balances explicit efficiency with implicit accuracy, resulting in smoother interactions between adjacent pixels, enhanced detail preservation, reduced numerical oscillations, and lower FID scores for the generated images. When $\theta = 1$, the pixel values at the current timestep depend solely on the values of adjacent pixels from the previous timestep, resulting in direct and rapid local information transfer between neighboring pixels. This leads to excessive smoothing of high-frequency details or incoherent local structures. While computationally efficient, the stability is constrained by the value of K , resulting in limited optimization of generation performance. When $\theta = 0$, the current pixel values depend entirely on the values of adjacent pixels at the current timestep, exhibiting strong global interdependence between neighboring pixels. This configuration suppresses high-frequency noise at the cost of sacrificing fine details, resulting in generated images with reduced diversity. Unless specific smoothness requirements are imposed, this approach is generally not adopted. Therefore, θ is uniformly set to 1/2 throughout our experiment.

In matrix \mathbf{A} , another critical parameter is the coefficient K . In order to deepen the understanding of model optimization, we study the effect of coefficient K on the model performance improvement. Figure 3 shows the effect of the change of coefficient K on the FID score of HDM. This image was obtained through training on the ImageNet dataset at 256×256 resolution.

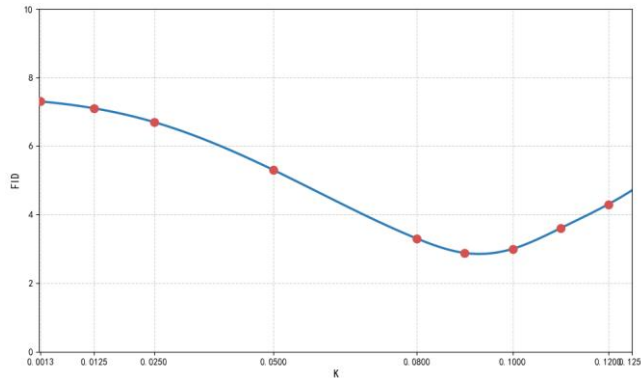


Fig. 3: The impact of the coefficient K on the FID score.

When $K = 0$, matrix \mathbf{A} reduces to an identity matrix, and the corresponding FID score equals that of the standard DDPM. When K is too small, the weights of the non-diagonal elements of matrix \mathbf{A} are

small, and the interactions between pixels are almost negligible. While high-frequency details can be largely preserved, the lack of inter-pixel cooperative optimization may result in isolated noise artifacts or locally incoherent regions. The optimization efficacy is not significantly pronounced. The monotonic increase in the K -value initially enhances the denoising capability of the model through the introduction of structured perturbations that conform to natural image degradation patterns, thereby improving generation quality and reducing the FID score. However, as K approaches the critical threshold of 0.125, the excessive attenuation of the central weighting coefficient leads to error accumulation during iterative updates, while the overly strong global dependencies between pixels induce numerical instability. This manifests as amplified high-frequency artifacts and compromised local consistency, coupled with excessive smoothing of critical high-frequency features, ultimately resulting in the observed rebound of the FID score. Values exceeding 0.125 are meaningless due to the aforementioned stability boundary condition, rendering further discussion of FID variations in this regime unnecessary.

Figure 3 demonstrates that K values between 0.08 and 0.11 enable the model to achieve optimal generation performance, with marginal further improvement beyond this range. In our experiments, $K = 0.095$. With both θ and K values determined, the formal experiments can commence. All other parameters remain consistent with DDPM.

Table 1 presents the Inception scores and FID scores on CIFAR-10. Our FID score is 3.05, demonstrating that our unconditional model exhibits superior sample quality compared to most models in the literature. The FID score is computed on the training set, which is the standard practice; when evaluated on the test set, the score is 3.63, which still surpasses the training set FID scores of many models reported in the literature. Both the training and testing processes utilized images with a resolution of 64×64 . For lower-dimensional images, the scarcity of local details results in global information (such as overall shape and color distribution) dominating, which is why the FID score did not decrease significantly.

Table 1. CIFAR10 results.

Model	FID ↓	IS ↑
Conditional		
EBM	37.8	8.31
BigGAN	14.72	9.23
StyleGAN2+ADA(V1)	2.66	10.07
Unconditional		
GatedPixel CN	65.92	4.61
PixelIQN	49.45	5.30
EBM	38.2	6.79
NCSN	25.31	8.88±0.13
SNGAN	21.60	8.23±0.06
SNGAN+DDLs	15.41	9.10±0.11
StyleGAN2+ADA(V1)	3.25	9.75 ± 0.1
DDPMs	3.16	9.47±0.12
Ours	3.05	9.79±0.07

Conducting training and testing solely on 64×64 resolution images is not rigorous. To validate that HDM also outperforms DDPM in generating high-dimensional images, additional tests were conducted on

256×256 images from the LSUN dataset and 256×256 images from the ImageNet dataset. Table 2 presents the FID scores obtained after training on the ImageNet dataset, demonstrating that HDM not only achieves better scores than DDPM but also outperforms subsequent models such as CDM and LDM. Furthermore, it outperforms the majority of models in AR.

Table 2. ImageNet 256×256 results.

Type	Model	FID ↓	IS ↑	Pre ↑	Rec ↑	#Para	#Step
GAN	BigGAN	6.95	224.5	0.89	0.38	112M	1
	GigaGan	3.45	225.50	0.84	0.61	569M	1
	StyleGan-XL	2.30	265.1	0.78	0.53	166M	1
Diff.	ADM	10.94	101.00	0.69	0.63	554M	250
	CDM	4.88	158.7	–	–	–	8100
	LDM-4-G	3.60	247.7	–	–	400M	250
	DiT-L/2	5.02	167.2	0.75	0.57	458M	250
	DiT-XL/2	2.27	278.2	0.83	0.57	675M	250
	Ours	2.89	221.02	0.78	0.56	376M	1000
Mask	MaskGIT	6.18	182.1	0.80	0.51	227M	8
	RCG (cond.)	3.49	215.5	–	–	502M	20
AR	VQGAN†	18.65	80.4	0.78	0.26	227M	256
	VQGAN	15.78	74.3	–	–	1.4B	256
	VQGAN-re	5.20	280.3	–	–	1.4B	256
	ViTVQ	4.17	175.1	–	–	1.7B	1024
	RQTran.	7.55	134.0	–	–	3.8B	68
	RQTran.-re	3.80	323.7	–	–	3.8B	68
	SPAE	4.41	133.03	–	–	–	100
	LlamaGen-B	5.46	193.61	0.83	0.45	111M	250
	LlamaGen-3B	2.18	263.33	0.81	0.58	3B	250
VAR	VAR-d16	3.30	274.4	0.84	0.51	310M	10
	VAR-d20	2.57	302.6	0.83	0.56	600M	10

Figures 4 and 5 illustrate the FID scores of HDM on the corresponding datasets from LSUN.



Fig. 4: LSUN Bridge samples. FID=4.22



Fig. 5: LSUN Church samples. FID=3.59

To provide a more intuitive comparison between HDM and DDPM, the generation results of both models can be evaluated using the same input image. During the forward noise-adding process, a controlled amount of noise is introduced to the input image. It is crucial to ensure that the image is not corrupted into pure noise, as this would lead to inconsistent final generated images. Figure 6 presents a comparison between the images generated by HDM and those generated by DDPM.

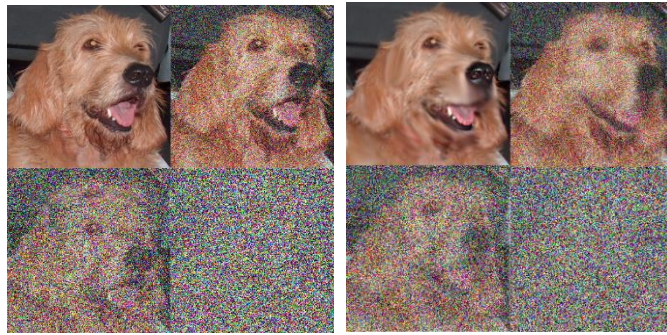


Fig. 6: Comparison of images generated by HDM (left) and DDPM (right).

As shown in Figure 6, HDM preserves more details, with the whiskers and mouth of the dog in the image exhibiting higher realism and better differentiation in similar regions.

To further validate the optimization of HDM in improving the quality of generated images, we conducted an ablation study. In the experiments, the matrix \mathbf{A} representing the positional and quantitative relationships between pixels was replaced with a random matrix, where each element was assigned a randomly generated weight, while ensuring that the input and output data of the diffusion and generation processes remained in vector or matrix form. Subsequently, DDPM, HDM, and the ablation experiment were trained and tested on the ImageNet 256×256 dataset, and the FID scores of each model as a function of the number of sampling steps are illustrated in Figure 7.

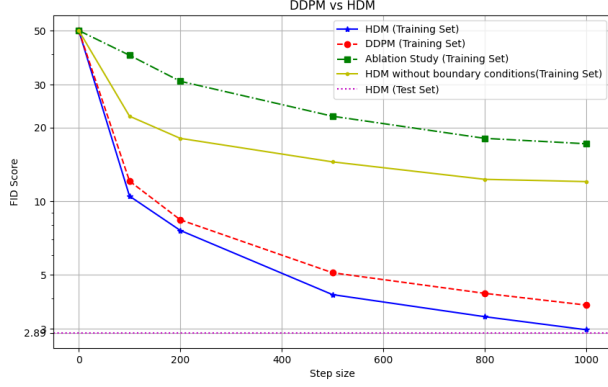


Fig. 7: The variation of FID with respect to the number of sampling steps.

As can be seen from the figure, merely reformulating the diffusion and generation processes in matrix form without incorporating quantitative and positional relationships does not improve the performance of DDPM. It is worth noting that selecting scientifically appropriate boundary conditions contributes to enhancing the quality of generated images. The relational matrix incorporated in HDM achieves optimization over DDPM. The initial FID score was set to 50 for graphical convenience, and by 100 steps, the FID scores of all three models had fallen below 50.

During the experiments, we observed that the generation time for HDM and DDPM differ, however, the specific comparison of time consumption was unclear. Therefore, to determine whether the generation process of HDM requires significantly more time, we conducted a comparative experiment. The figure below illustrates the impact of the coefficient K on the generation time of HDM.

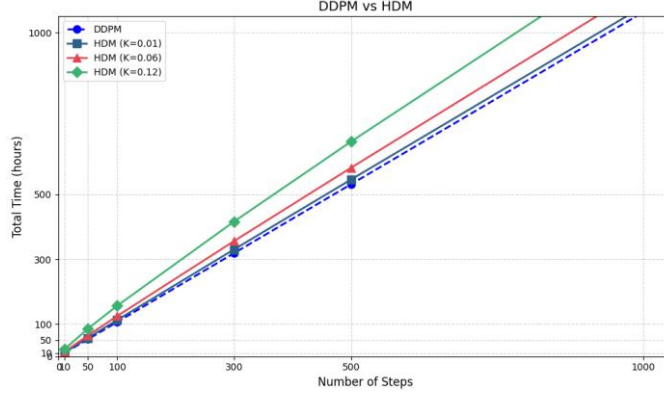


Fig. 8 Comparison of generation time among the models.

As can be observed from the figure, as the parameter K gradually increases, the time required for the model to generate images also increases significantly. This is particularly evident when the image resolution is high, as the matrix dimensionality substantially increases, causing the matrix to approach a dense matrix and leading to a notable rise in computational complexity. When the value of K is not excessively large, the time required for HDM is comparable to that of DDPM, and GPU acceleration can be utilized to expedite matrix operations. Therefore, in the experiments, to ensure image quality while optimizing performance, the optimal choice for the parameter K lies within the range of 0.08 and 0.1.

5 CONCLUSIONS

In response to the current extensive image processing demands, this study proposes a diffusion model optimized via the heat equation. By incorporating pixel-level relationships into both the diffusion and

generation processes of DDPM, the model enhances its capability to preserve and process fine details, particularly in high-resolution image tasks. The incorporation of the discretized heat equation enables the diffusion model to process data in matrix form. Although the model processes a larger volume of data, the matrix-based framework offers the advantages of parallel computation and reduced memory overhead. The model efficiently handles large-scale matrix operations, achieving enhanced fine-grained feature processing with only marginal computational overhead. Our method demonstrates superior capability in distinguishing highly similar objects compared to DDPM, CDM, and LDM models, as experimentally verified. The image generation also exhibits finer details compared to most AR models and Mask.

REFERENCES

- [1] Ho, J., Jain, A., and Abbeel, P. Denoising diffusion probabilistic models. In NeurIPS, 2020.
- [2] Song, Jiaming et al. "Denoising Diffusion Implicit Models." arXiv abs/2010.02502 (2020): n. pag.
- [3] Tong Che, Ruixiang Zhang, Jascha Sohl-Dickstein, Hugo Larochelle, Liam Paull, Yuan Cao, and Yoshua Bengio. Your GAN is secretly an energy-based model and you should use discriminator driven latent sampling. arXiv preprint arXiv:2003.06060, 2020.
- [4] Karras, T., Aittala, M., Aila, T., and Laine, S. Elucidating the design space of diffusion-based generative models, 2022. URL <https://arxiv.org/abs/2206.00364>. Arxiv 2206.00364.
- [5] Kong, X., Brekelmans, R., and Steeg, G. V. Information-theoretic diffusion. In ICLR, 2023.
- [6] Song, Y., Sohl-Dickstein, J., Kingma, D. P., Kumar, A., Ermon, S., and Pool, B. Score-based generative modeling through stochastic differential equations. In ICLR, 2021.
- [7] T. S. W. Stevens, O. Nolan, J. -L. Robert and R. J. G. Van Sloun, "Sequential Posterior Sampling with Diffusion Models," ICASSP 2025 - 2025 IEEE International Conference on Acoustics, Speech and Signal Processing (ICASSP), Hyderabad, India, 2025, pp. 1-5, doi:10.1109/ICASSP49660.2025.10889752.
- [8] Z. Huang, K. Wang, Y. Xiao and Z. Xiang, "Research and Application of LSTM Model and Diffusion Model," 2024 IEEE 2nd International Conference on Sensors, Electronics and Computer Engineering (ICSECE), Jinzhou, China, 2024, pp. 875-878, doi:10.1109/ICSECE61636.2024.10729552.
- [9] H. Čeović, M. Šilić, G. Delač and K. Vladimir, "An Overview of Diffusion Models for Text Generation," 2023 46th MIPRO ICT and Electronics Convention (MIPRO), Opatija, Croatia, 2023, pp. 941-946, doi:10.23919/MIPRO57284.2023.10159911.
- [10] Nichol, A., Dhariwal, P., Ramesh, A., Shyam, P., Mishkin, P., McGrew, B., Sutskever, I., and Chen, M. Glide: Towards photorealistic image generation and editing with text-guided diffusion models. arXiv preprint arXiv:2112.10741, 2021.
- [11] Kawar, B., Elad, M., Ermon, S., and Song, J. Denoising diffusion restoration models. In Advances in Neural Information Processing Systems, 2022.
- [12] F. Bao, C. Xiang, G. Yue, G. He, H. Zhu, K. Zheng, M. Zhao, S. Liu, Y. Wang, and J. Zhu. Vidu: a highly consistent, dynamic and skilled text-to-video generator with diffusion models. arXiv preprint arXiv:2405.04233, 2024.
- [13] Rombach, R., Blattmann, A., Lorenz, D., Esser, P., and Ommer, B. High-resolution image synthesis with latent diffusion models. In Proceedings of the IEEE/CVF Conference on Computer Vision and Pattern Recognition, pp. 10684–10695, 2022.
- [14] E. Cho, J. Bang and M. Rhu, "Characterization and Analysis of Text-to-Image Diffusion Models," in IEEE Computer Architecture Letters, vol. 23, no. 2, pp. 227-230, July-Dec. 2024, doi: 10.1109/LCA.2024.3466118.
- [15] Yutong Bai, Xinyang Geng, Karttikeya Mangalam, Amir Bar, Alan L Yuille, Trevor Darrell, Jitendra Malik, and Alexei A Efros. Sequential modeling enables scalable learning for large vision models. In Proceedings of the IEEE/CVF Conference on Computer Vision and Pattern Recognition, pp. 22861–22872, 2024b.

- [16] Jacob Austin, Daniel D Johnson, Jonathan Ho, Daniel Tarlow, and Rianne van den Berg. 2021. Structured denoising diffusion models in discrete state-spaces. In *Advances in Neural Information Processing Systems*.
- [17] Saharia, C., Chan, W., Saxena, S., Li, L., Whang, J., Denton, E., Ghasemipour, S. K. S., Ayan, B. K., Mahdavi, S. S., Lopes, R. G., et al. Photorealistic text-to-image diffusion models with deep language understanding. *arXiv preprint arXiv:2205.11487*, 2022.
- [18] Heat Transfer - *Advances in Fundamentals and Applications*. 2024. doi:10.5772/INTECHOPEN.107587.
- [19] Zheng, H., Nie, W., Vahdat, A., Azizzadenesheli, K., and Anandkumar, A. Fast sampling of diffusion models via operator learning. *arXiv preprint arXiv:2211.13449*, 2022.
- [20] Cheng Lu, Yuhao Zhou, Fan Bao, Jianfei Chen, Chongxuan Li, and Jun Zhu. Dpm-solver: A fast ode solver for diffusion probabilistic model sampling in around 10 steps. *arXiv preprint arXiv:2206.00927*, 2022a.
- [21] Tero Karras, Samuli Laine, Miika Aittala, Janne Hellsten, Jaakko Lehtinen, and Timo Aila. Analyzing and improving the image quality of StyleGAN. In *Proceedings of the IEEE/CVF Conference on Computer Vision and Pattern Recognition*, pages 8110–8119, 2020.
- [22] Chenlin Meng, Robin Rombach, Ruiqi Gao, Diederik Kingma, Stefano Ermon, Jonathan Ho, and Tim Salimans. On distillation of guided diffusion models. In *Proceedings of the IEEE/CVF Conference on Computer Vision and Pattern Recognition*, pp. 14297–14306, 2023.
- [23] Dustin Podell, Zion English, Kyle Lacey, Andreas Blattmann, Tim Dockhorn, Jonas Müller, Joe Penna, and Robin Rombach. Sdxl: improving latent diffusion models for high-resolution image synthesis. *arXiv preprint arXiv:2307.01952*, 2023.
- [24] Robin Rombach, Andreas Blattmann, Dominik Lorenz, Patrick Esser, and Björn Ommer. High-resolution image synthesis with latent diffusion models. In *Proceedings of the IEEE/CVF Conference on Computer Vision and Pattern Recognition*, pp. 10684–10695, 2022.